



THE UNIVERSITY *of* EDINBURGH

Edinburgh Research Explorer

## Modeling homogeneous ignition processes of clustering solid particle clouds in isotropic turbulence

**Citation for published version:**

Farmand, P, Nicolai, H, Usman, M, Berger, L, Attili, A, Gauding, M, Hasse, C & Pitsch, H 2024, 'Modeling homogeneous ignition processes of clustering solid particle clouds in isotropic turbulence', *Fuel*, vol. 371, no. Part B, 132054. <https://doi.org/10.1016/j.fuel.2024.132054>

**Digital Object Identifier (DOI):**

[10.1016/j.fuel.2024.132054](https://doi.org/10.1016/j.fuel.2024.132054)

**Link:**

[Link to publication record in Edinburgh Research Explorer](#)

**Document Version:**

Peer reviewed version

**Published In:**

Fuel

**General rights**

Copyright for the publications made accessible via the Edinburgh Research Explorer is retained by the author(s) and / or other copyright owners and it is a condition of accessing these publications that users recognise and abide by the legal requirements associated with these rights.

**Take down policy**

The University of Edinburgh has made every reasonable effort to ensure that Edinburgh Research Explorer content complies with UK legislation. If you believe that the public display of this file breaches copyright please contact [openaccess@ed.ac.uk](mailto:openaccess@ed.ac.uk) providing details, and we will remove access to the work immediately and investigate your claim.



# Modeling homogeneous ignition processes of clustering solid particle clouds in isotropic turbulence

Pooria Farmand<sup>a,\*</sup>, Hendrik Nicolai<sup>b</sup>, Muhammad Usman<sup>a</sup>, Lukas Berger<sup>a</sup>, Antonio Attili<sup>c</sup>, Michael Gauding<sup>a</sup>, Christian Hasse<sup>b</sup>, Heinz Pitsch<sup>a</sup>

<sup>a</sup>*RWTH Aachen University, Faculty of Mechanical Engineering, Institute for Combustion Technology, Templergraben 64, 52056 Aachen, Germany*

<sup>b</sup>*Technical University of Darmstadt, Department of Mechanical Engineering, Simulation of reactive Thermo-Fluid Systems, Otto-Berndt-Straße 2, 64287 Darmstadt, Germany*

<sup>c</sup>*University of Edinburgh, School of Engineering, Institute of Multiscale Thermofluids, The King's Buildings, Mayfield Road, Edinburgh, EH9 3FD, United Kingdom*

---

## Abstract

The objective of this study is to numerically investigate the ignition and combustion of pulverized solid fuels in turbulent conditions and to assess different modeling strategies relevant to large-eddy simulations (LES). The investigations show that due to the high Stokes number of solid particles, they do not necessarily follow the flow. At Stokes numbers around unity, particle-turbulence interactions can lead to particle clustering and change the ignition behavior. According to observations, ignition is most likely to happen outside the formed clusters, where suitable thermo-chemical conditions exist. To study this behavior, direct numerical simulations (DNS) of reactive particles in turbulent conditions employing detailed kinetics for solid and gas phases were performed. Pulverized fuel combustion was modeled using the point-particle approximation to represent the dispersed phase in an

---

\*Corresponding author

*Email address:* `p.farmand@itv.rwth-aachen.de` (Pooria Farmand)

Eulerian-Lagrangian framework. Isotropic turbulence was employed to investigate the influence of particle clustering on the ignition process. After investigating the physical aspects of the ignition process, the DNS dataset was used as a benchmark for evaluating the reduced-order flamelet models usually employed in LES of pulverized fuel combustion during the ignition process. The flamelet model performance in predicting the selected quantity of interest was compared to the DNS data. An error decomposition was performed using the optimal estimator concept. Finally, the prediction accuracy of presumed PDFs is evaluated by calculating the errors in predicting the quantity of interest using different PDFs compared to the predictions using the accurate sub-filter joint distribution of the DNS data. The *a priori* model assessment showed the best performance for the model, especially inside particle clusters, when using mixture fraction, progress variable, and enthalpy as flamelet tabulation input parameters and employing the presumed  $\beta$ -PDF for mixture fraction.

*Keywords:*

Isotropic turbulence, Pulverized fuel, Ignition and combustion, DNS, Flamelet model assessment, Subgrid PDF

---

## 1. Introduction

2 Solid fuel combustion remains a principal technology for producing elec-  
3 tricity, as it has reached a matured technological state and possesses reliable  
4 supply chains with the possibility of a change from conventional to bio-fuels.  
5 However, burning solid fuels, such as pulverized coal or biomass, can be a ma-  
6 jor source of pollutants and CO<sub>2</sub>. Hence, improvements in system efficiency

7 and carbon capture and storage (CCS) methods to reduce the environmental  
8 impact are actively researched. Experimental techniques for studying solid  
9 fuel combustion remain challenging due to the hostile environment in boilers  
10 and limited optical access [1]. Therefore, numerical simulations provide an  
11 alternative to enable insights into the underlying complex multi-physics and  
12 multi-scale processes.

13 For predictive modeling of solid fuel combustion, three main modeling  
14 pillars can be identified: solid fuel conversion, turbulent mixing and heat  
15 transfer, as well as turbulence-chemistry interactions [1]. For solid-fuel sub-  
16 models, most numerical studies rely on simplified models, whose parameters  
17 must be adjusted to capture fuel type changes or operating conditions accu-  
18 rately [1]. However, recent numerical studies have employed more detailed  
19 solid fuel models, such as the chemical percolation devolatilization (CPD) [2]  
20 or the CRECK-S [3] models [4–7]. These models enable a more detailed de-  
21 scription of the solid particle conversion process for various fuels and a vast  
22 range of conditions by including more detailed information about the fuel,  
23 such as its molecular structure [8].

24 To capture the turbulent flow environment in pulverized coal combustion  
25 (PCC), traditionally Reynolds-averaged Navier-Stokes (RANS) approaches  
26 have been used. However, with the advancements of computational resources,  
27 the application of scale-resolving techniques became feasible, offering higher  
28 accuracy for predictive simulations [1, 9]. In recent years, large-eddy sim-  
29 ulations (LES) have been successfully extended to study PCC and used in  
30 several studies [10–14]. These advancements in simulation techniques have  
31 provided valuable insights into the interactions between turbulent motion

32 and combustion characteristics of pulverized fuels.

33 In the context of turbulence-chemistry interactions, state-of-the-art mod-  
34 els are often based on a global description of gas-phase chemistry employing  
35 a limited number of reactions. Turbulence closure for these models is com-  
36 monly achieved by the eddy-breakup model (EBM) or the eddy-dissipation  
37 concept (EDC) [1]. To enable a more detailed representation of the com-  
38 plex gas mixtures released from solid particles, recent efforts have focused on  
39 extending flamelet-based modeling approaches specifically for solid fuel com-  
40 bustion [15]. With different focuses, several authors have explored flamelet-  
41 based tabulation approaches with applications to various configurations rang-  
42 ing from single particle and particle group combustion [16, 17] to pilot-  
43 scale furnaces [11–14]. Flamelet-based approaches offer the advantage of  
44 using detailed chemical mechanisms at low computational cost. They have  
45 proven effective in capturing both global characteristics, such as ignition  
46 processes [16, 17], flame structures [12, 13], and local species concentra-  
47 tions [11, 14]. Particularly, in combination with LES, flamelet tabulation has  
48 shown promising results, although appropriate subgrid closures are necessary  
49 to ensure maintaining accuracy. To address the closure problem, commonly  
50 employed methods involve the use of presumed filtered density functions [1].

51 These presumed filter density functions can be developed and assessed  
52 by detailed reference data [18], such as direct numerical simulations (DNS),  
53 where all turbulence scales and all near- and intra-particle processes are re-  
54 solved by the numerical grid. Resolving all physical processes, including the  
55 particle boundary layers, became feasible within recent years [19, 20], but  
56 is still restricted to very few particles ( $\mathcal{O}(10)$ ) and relatively low Reynolds

57 numbers. Therefore, an alternative resolved flow simulation approach, the  
58 so-called carrier-phase DNS (CP-DNS), is commonly employed for solid fuels  
59 to enable fundamental insights into multiple interacting reactive particles.  
60 For this approach, the DNS resolves only the scales of the carrier phase,  
61 and the boundary layers around the individual particles while their impacts  
62 on the resolved scales are modeled. Using CP-DNS, Messig et al. [21] and  
63 Wen et al. [22] investigated laminar counterflow burners and performed de-  
64 tailed flame structure analyses for flamelet modeling; turbulent multi-phase  
65 jet burners were investigated by Luo et al. [23], Bai et al. [24], and Hara  
66 et al. [25]. These studies revealed that three distinctly different flame zones  
67 can be identified [24] and that both premixed and non-premixed combus-  
68 tion modes can appear [25]. Similar conclusions were drawn in the recent  
69 CP-DNS of a turbulent mixing layer resembling the condition of the inner  
70 recirculation zone of a swirled PCC boiler [26]. The latter dataset was exten-  
71 sively employed to evaluate different flamelet modeling approaches [27–29].  
72 A more simplified configuration of coal particle clouds in decaying turbulence  
73 was investigated by Brosh et al. [30]. They showed a strong dependency of  
74 homogenous ignition on particle density and clustering. Similar findings have  
75 been published for heterogeneous char conversion in forced isotropic turbu-  
76 lence by Krüger et al. [31]. The authors investigated turbulence-induced  
77 particle clustering and reported significant reductions in particle reactivity  
78 and char conversion rate inside particle clusters. The observed clustering  
79 effects were found to be strongly influenced by the particle Stokes number,  
80 which is the ratio of the characteristic time of a particle to the characteristic  
81 time of the flow, as indicated in the aforementioned studies. Considering that

82 clustering occurs in larger-scale burners, it becomes crucial to investigate the  
83 performance of recently developed flamelet models and subgrid closures in  
84 the context of particle clustering.

85 Therefore, the objective of this work is to study the modeling of the  
86 homogeneous ignition process and volatile combustion of solid fuel particles  
87 in isotropic turbulence under conditions favoring particle clustering, which is  
88 typically observed in pulverized solid fuel burners. Particularly, the effect of  
89 particle-chemistry-turbulence interactions on the local ignition process and  
90 in clustering particle clouds is investigated. Therefore, modeling strategies  
91 for both the reduction of the gas-phase reactions by an FPV approach and  
92 the required closure for the filtered variables in the context of LES are studied  
93 in homogenous isotropic turbulence-induced particle clusters. The optimal  
94 estimator concept is employed to determine modeling errors and provide an  
95 effective modeling strategy for turbulent solid-fuel combustion.

96 The remainder of the paper is structured as follows. First, in Section 2,  
97 the employed numerical framework and the models to be assessed are briefly  
98 introduced. This is followed by a short description of the numerical setup  
99 and the boundary conditions for the DNS in section 3. In Section 4, first, the  
100 physical effects of the employed configuration are presented, then a combined  
101 LES-FPV approach is assessed in an *a priori* analysis.

## 102 **2. Modeling framework and methods**

### 103 *2.1. Multi-phase modeling*

104 In this study, the ignition and combustion process of pulverized coal par-  
105 ticle clouds is represented by an Eulerian-Lagrangian approach. The conser-

106 vation of mass, momentum, species, and energy between the Lagrangian and  
107 Eulerian frameworks is ensured by a two-way coupling. Utilizing the two-way  
108 coupling also ensures the particle-fluid-chemistry interactions by distribut-  
109 ing the particles' source terms in the Eulerian phase and calculating the  
110 gas-phase quantities at the particles' location. The detailed description of  
111 the models and the equations for the Eulerian and Lagrangian formulations  
112 can be found in Farmand et al. [5] and Farazi et al. [32]. The accuracy of  
113 the applied models and methodologies have been validated against experi-  
114 mentally measured data for ignition times in different laminar configurations  
115 in earlier works [5, 32–34]. One particular focus of these studies was on  
116 properly capturing particle movement and ignition of point particles on DNS  
117 grids through a Gaussian kernel source term distribution. Chemical reac-  
118 tions in the gas phase are described employing finite-rate chemistry adopting  
119 a mechanism suitable for coal and biomass combustion with 68 species and  
120 906 reactions, which has been validated for different fuels in both air and oxy-  
121 fuel atmospheres [35], and has been used in previous studies [4, 5, 36, 37].

122 Particle dynamics are modeled in a Lagrangian framework using the  
123 point-particle assumption solving equations for trajectory, velocity, mass,  
124 and temperature as described in previous works [5, 32, 38]. In order to have  
125 a detailed description of the solid particle conversion, the chemical percola-  
126 tion devolatilization (CPD) model, which is one of the most detailed models  
127 for solid kinetics, is used to describe the volatile release from the solid parti-  
128 cles based on the molecular structure of the fuel and considers the solid fuel  
129 as a complex network of the large aromatic hydrocarbon monomers and the  
130 bridges, in which bonds are broken by the external energy at each tempera-



131 ture level. This model, as described in detail in [2, 8, 39], takes into account  
132 the dynamic behavior of the devolatilization process by determining total  
133 released mass as well as its composition in light gases and tar. In the present  
134 study, light gases consist of  $\text{CH}_4$ ,  $\text{CO}_2$ ,  $\text{CO}$ ,  $\text{H}_2\text{O}$ , and other gases, which  
135 are assumed to be  $\text{C}_2\text{H}_2$  similar to the assumption by Jimenez and Gonzalo-  
136 Tirado [40]. The released tars are assumed to solely consist of  $\text{C}_2\text{H}_2$ . To  
137 reduce the level of complexity in the model assessment procedure, similar  
138 to [5], a fixed volatile composition assumption (FVC) is employed for the  
139 particle devolatilization in the CPD model. The FVC is calculated based  
140 on the time-averaged values of each volatile species' mass compared to the  
141 total released mass from the particle [4]. The resulting set of fixed volatile  
142 mass fractions is  $Y_{\text{CH}_4} = 0.057$ ,  $Y_{\text{CO}_2} = 0.072$ ,  $Y_{\text{CO}} = 0.087$ ,  $Y_{\text{H}_2\text{O}} = 0.268$ ,  
143 and  $Y_{\text{C}_2\text{H}_2} = 0.516$ . Assuming a fixed volatile composition neglects the rela-  
144 tionship between the change in particle heating rate and the volatile release,  
145 which is commonly made for flamelet modeling in the LES of solid pulverized  
146 fuel flames [4] and was found to only marginally affect ignition [5].

147 To solve the governing equations in isotropic turbulence, the in-house  
148 structured finite difference solver CIAO is used. In CIAO, the Eulerian equa-  
149 tions are solved using a semi-implicit scheme with second-order accuracy in  
150 space and time. The scalar transport is solved using the fifth-order WENO  
151 scheme for the convective terms and a second-order central difference scheme  
152 for the diffusive terms. The chemistry is solved using the finite rate chem-  
153 istry method using the CVODE solver [5, 32]. The particles are advanced in  
154 time utilizing a two-stage Runge-Kutta solver with second-order accuracy to  
155 update the dispersed phase state, position, and source terms for the Eulerian

156 equations. The reader is referred to previous works for specific details on the  
157 numerical implementation [5, 32].

## 158 2.2. Flamelet library for a priori analysis

159 To model the turbulent reacting gas-phase in solid fuel combustion, flamelet-  
160 based tabulation methods are gaining attraction due to the possibility of in-  
161 cluding detailed kinetics in large-scale simulations. In this work, flamelet ta-  
162 bles, which are used for the *a priori* model assessment in post-processing, are  
163 built from counterflow-diffusion flamelets, which matches the non-premixed  
164 nature of combustion in the current study configuration. These are solved in  
165 physical coordinates using Cantera [41], assuming unity Lewis numbers for  
166 all species, which is a common assumption in PCC (e.g., [4, 14]). The same  
167 gas-phase kinetic model as for the DNS is used to calculate the flamelets [35].  
168 During the flamelet calculation, the strain rate is varied by changing the in-  
169 flow boundary conditions. For the tabulation process, the varying strain  
170 rates are mapped onto a progress variable ( $C$ ) [42], which represents the  
171 combustion progress.

172 To take into consideration heat losses in the gas-phase caused by par-  
173 ticles and radiative heat transfer, the enthalpy  $h$  (sensible plus chemical)  
174 is introduced as an additional table dimension, and flamelets with different  
175 enthalpy levels are computed. For higher enthalpy values, the temperatures  
176 of the oxidizer and fuel are increased (from 300 K up to 1500 K). To obtain  
177 lower enthalpies, the source term in the temperature equation in Cantera is  
178 rescaled, as proposed by several authors [4, 14, 43]. Below a certain enthalpy  
179 level, no flamelet solution can be obtained. Here, a linear extrapolation to  
180 300 K is used to complete the composition space [16, 44].

181 In the flamelet tabulation, normalized values for  $h$  and  $C$  based on the  
 182 lower and upper limits of the flamelet table, which represents the lowest and  
 183 highest possible temperature for the composition space, are employed [45]:

$$C_n = \frac{C - C_{\min}(h, Z)}{C_{\max}(h, Z) - C_{\min}(h, Z)}, \quad (1)$$

184

$$h_n = \frac{h - h_{\min}(Z)}{h_{\max}(Z) - h_{\min}(Z)}. \quad (2)$$

185 This will also improve the statistical independence between table input pa-  
 186 rameters [42, 46] and enable the possibility of evaluating different presumed  
 187 PDF shapes for all input parameters when coupled to LES.

188 When the tabulated chemistry is coupled to LES, modeling of the sub-  
 189 grid filtered/probability density functions (FDF/PDF) is required since only  
 190 Favre-filtered scalars are available for the table access [42]. Closure can be  
 191 obtained through the joint-scalar-PDF in composition space. This involves  
 192 integrating the joint-scalar-PDF over the composition space to obtain the  
 193 filtered quantity of interest as

$$\bar{\Psi} = \int \Psi(Z, C_n, h_n, \dots) \tilde{P}(Z, C_n, h_n, \dots) dZ dC_n dh_n \dots, \quad (3)$$

194 where the density-weighted PDF  $\tilde{P}$  follows from the Favre-averaging proce-  
 195 dure. Since the joint-scalar-PDF is computationally expensive to calculate  
 196 during runtime, presumed PDF closures are commonly employed. The PDF  
 197 has to be parametrized by the moments of the distribution, and it is often  
 198 assumed that the PDF can be represented by its first two moments. Since  
 199 prescribing a feasible presumed PDF for the joint PDF of multiple scalars  
 200 is very challenging, the simplified assumption of statistical independence be-  
 201 tween the scalar dimensions of the joint PDF is often used [14, 18]. As a

202 result, the representation of the joint PDF of multiple scalars in composi-  
 203 tion space can be facilitated to the product of the individual marginal scalar  
 204 PDFs as:

$$\bar{\Psi} = \int \Psi(Z, C_n, h_n) \tilde{P}(Z, \tilde{Z}, \widetilde{Z''^2}) \tilde{P}(C_n, \tilde{C}_n, \widetilde{C_n''^2}) \tilde{P}(h_n, \tilde{h}_n, \widetilde{h_n''^2}) dZ dC_n dh_n \quad (4)$$

205 Mostly, in tabulated flamelet models used in pulverized fuel combustion, all  
 206 scalars besides the mixture fraction are modeled by a  $\delta$  function, and the  
 207 sub-grid PDF of the mixture fraction is approximated by top-hat [6, 47] or  
 208  $\beta$  [4, 14] distribution functions.

### 209 2.3. Error decomposition analysis

210 The modeling of unclosed terms in partial differential equations typically  
 211 involves two steps: First, a set of known quantities needs to be specified as  
 212 input parameters for a model, and second, a specific functional form needs  
 213 to be defined to model the unclosed terms by the input parameters [48–50].  
 214 Each of these steps introduces errors that need to be carefully investigated  
 215 in the model assessment process. The error corresponding to the first step  
 216 is known as the irreducible error, and the error corresponding to the second  
 217 step is referred to as the functional error. Typically, the total modeling  
 218 error, which involves both irreducible and functional errors, is calculated by  
 219 the overall difference between quantities of interest calculated by the model  
 220 and the DNS. The quadratic total modeling error over all  $N$  data points is  
 221 defined as

$$\epsilon_{\text{tot}}^2(\phi) = \frac{1}{N} \sum_{i=1}^N (\phi_{i,\text{DNS}} - \phi_{i,\text{Model}})^2, \quad (5)$$

222 where  $\epsilon_{\text{tot}}(\phi)$  is the average value of the total modeling error for a quantity  
 223 of interest  $\phi$  over all  $N$  data points. The general idea of the optimal es-  
 224 timator concept is to determine for a given parameter set  $\Pi$ , the mean of  
 225 a quantity of interest  $\phi$  conditioned on the set of parameters  $\langle \phi | \Pi \rangle$  and  
 226 obtain a measure for the scatter of the quantity of interest with respect to  
 227  $\Pi$ . This is the minimum error possible after choosing the parameters set and  
 228 is called irreducible error. In this study, an artificial neural network (ANN)  
 229 with a single hidden layer is used to calculate the optimal estimator and the  
 230 irreducible error, which is computationally efficient, even when using a large  
 231 number of input parameters [48].

232 Using the optimal estimator and the irreducible error concepts, the total  
 233 modeling error can be decomposed into irreducible and functional errors [48],  
 234 in which the functional error corresponds to the performance of the model  
 235 for a given input parameter set

$$\epsilon_{\text{tot}}^2(\Pi) = \epsilon_{\text{irr}}^2(\Pi) + \epsilon_{\text{funct}}^2(\Pi), \quad (6)$$

236 where  $\Pi$  is a set of known parameters used as input of the model. Formally,  
 237 the irreducible error is given as

$$\epsilon_{\text{irr}}^2 = \langle (Q_{\text{int}} - \langle Q_{\text{int}} | \Pi \rangle)^2 \rangle \quad (7)$$

238 In the following, irreducible error  $\epsilon_{\text{irr}}$  and the error caused by the functional  
 239 form of the model  $\epsilon_{\text{funct}}$ , as defined by equation (6), will be discussed sepa-  
 240 rately for identifying the potential for model improvements.

#### 241 *2.4. Quantifying preferential concentration/clustering*

242 When the particles are exposed to turbulence, their trajectory depends  
 243 on the turbulent intensity and particle inertia. This can lead to a local in-

244 crease in the particle number density at specific locations in the field, which  
 245 is known as preferential concentration or clustering [51, 52]. To identify the  
 246 formed clusters, the three-dimensional Voronoi tessellation method is em-  
 247 ployed [53]. In this method, the 3D particle field is discretized by Voronoi  
 248 diagrams created by the half-plane intersection algorithm between each two  
 249 particles in the field. This results in a specific volume around each particle,  
 250 called Voronoi cells, as described in [53]. The size of each Voronoi cell is  
 251 inversely related to the local concentration of the particles in a certain loca-  
 252 tion in the field [54]. After discretizing the domain by the Voronoi cells, the  
 253 clustering limit  $V_C$  can be obtained by comparing the normalized Voronoi vol-  
 254 ume distribution in the clustered field  $P(V/\bar{V})$  with a randomly distributed  
 255 particle field  $P(V_R/\bar{V})$ , in which  $\bar{V}$  is the mean Voronoi cell volume in the  
 256 selected field, which is calculated based on the Voronoi volume around each  
 257 particle as described in [53].  $V_C$  can be calculated when  $P(V/\bar{V}) = P(V_R/\bar{V})$ .  
 258 A more detailed description of the method can be found in Obligado et al.  
 259 [52] and Monchaux et al. [53]. After performing the Voronoi algorithm as  
 260 shown in Fig. 1a, a particle can be a member of a cluster when the respective  
 261 Voronoi volume around the particle is smaller than the calculated clustering  
 262 limit ( $V_C$ ). As a result, the cluster members can be identified as shown in  
 263 Fig. 1b.

### 264 3. Numerical setup and boundary conditions

265 In order to reduce the complexity caused by mean shear forces, it is  
 266 preferred to keep the turbulence fluctuations statistically uniform so that  
 267 all particles are subjected to the same turbulence statistics. Therefore, the

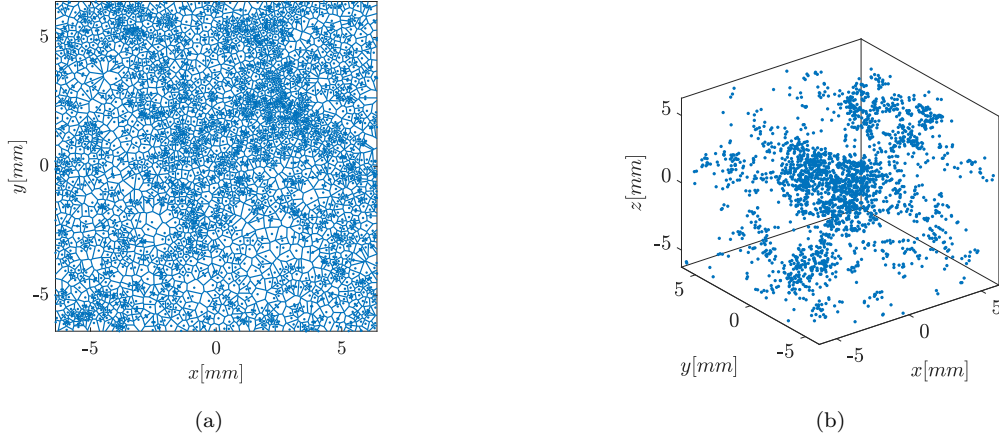


Fig. 1. a) Voronoi tessellation diagram for the 2D slice of the box b) Cluster member particles filtered by the Voronoi algorithm at the initial time of the clustering.

268 homogeneous isotropic turbulent (HIT) configuration within a box with pe-  
 269 riodic boundary conditions in all directions is chosen. Due to the absence  
 270 of mean gradients, HIT has no turbulence production, and, as a result, tur-  
 271 bulence decays in time. To investigate the effect of turbulence interactions  
 272 on the ignition and the combustion process, a pre-computed fully developed  
 273 HIT field with a linear forcing in physical space [55] is used as initial con-  
 274 ditions to keep turbulence in a statistically steady state. Simulations were  
 275 performed within a region with the physical size of  $12.8 \text{ mm} \times 12.8 \text{ mm} \times$   
 276  $12.8 \text{ mm}$  with periodic boundary conditions in all directions. The domain  
 277 size is discretized with a three-dimensional cartesian mesh with a resolution  
 278 of  $\Delta x = 50 \mu\text{m}$ . Since the particle clustering effect on ignition is one of the  
 279 main aspects of this study, turbulence characteristics and dispersed phase  
 280 size have been chosen such that particle clustering can be observed. These  
 281 conditions are representative of smaller-scale turbulent fluctuations under

282 practically relevant conditions [7, 26].

283 Particle clustering typically occurs when the characteristic time of the  
284 particles is on the same order as the flow time scale and is defined by the  
285 Stokes number. For Stokes numbers around unity, particles tend to form  
286 clusters, resulting in regions almost void of particles [56]. The Stokes number  
287 defined with the Kolmogorov time scale is given as

$$St = \frac{\rho_{\text{prt}} d_{\text{prt}}^2}{18 \rho_g \eta^2}. \quad (8)$$

288 A forced isotropic turbulent field with  $Re_\lambda \simeq 30$  and the Kolmogorov length  
289 scale  $\eta \simeq 100 \mu\text{m}$  has been chosen. The dispersed phase consists of 10,000  
290 particles of Colombian coal with  $d_{\text{prt}} = 20 \mu\text{m}$  and  $T_{\text{prt},0} = 300 \text{K}$  and with  
291 apparent density of  $700 \text{kg/m}^3$ . The coal properties can be found in [5]. Non-  
292 reactive particles are first randomly distributed in the box filled with air with  
293 20% oxygen and an initial gas temperature of  $T_{\text{g},0} = 1500 \text{K}$ , which is rele-  
294 vant to practical PCC applications. Based on equation (8), these conditions  
295 lead to an initial Stokes number of  $St \simeq 5$ , for which a clustering behavior  
296 in particle clouds motion is expected [57]. Finally, the reactive simulation  
297 starts after particle clusters have fully formed in a non-reactive HIT field  
298 to investigate the effect of particle clustering on the homogeneous ignition  
299 process. The employed forced isotropic turbulence ensures maintaining the  
300 same turbulence statistics during non-reactive and reactive simulations as  
301 summarized in [Appendix A](#).

302 To quantify the ignition process, an ignition criterion needs to be de-  
303 fined. Typically, in joint numerical-experimental studies, a certain OH rad-  
304 ical threshold is chosen as an ignition identifier based on OH-LIF measure-  
305 ments [5, 34]. In the current study, due to non-existing experimental mea-



306 surements for the current complex configuration, the same definition, used in  
307 previous studies [5, 16] to quantify the ignition process was used to have a re-  
308 alistic benchmark for the analysis. This definition has been validated against  
309 the experimentally measured ignition delay time in previous works. As a re-  
310 sult, the ignition onset is defined as the time when 10% of the maximum OH  
311 mass fraction during the entire combustion process is reached.

## 312 4. Results and discussion

313 In the following sections, first, the physical aspects of the ignition of  
314 clustering particles in isotropic turbulence and the ignitability condition are  
315 investigated. Then, the available models and their applicability for the igni-  
316 tion prediction in the clustering particle clouds are assessed.

### 317 4.1. Ignition process of clustering particles in isotropic turbulence

318 Figure 2 shows the evolution of the ignited regions in the computational  
319 domain over time. As shown in Fig. 2a, various ignition kernels are formed at  
320 various locations within the field where favorable thermo-chemical conditions  
321 for ignition exist. This process continues with the ignition of the adjacent  
322 regions due to the growth and merging of individual ignited regions until the  
323 whole domain is ignited and a continuous flame is established. The transition  
324 from the auto-ignition regime to the flame front propagation mode, which  
325 in this study is referred to as interaction ignition [58], can be quantified by  
326 investigating the time evolution of the ignited regions in the field as shown  
327 in Fig. 2.

328 Figure 2a also indicates preferential particle concentration, also known as  
329 particle clustering. To further investigate this observation, Voronoi regions

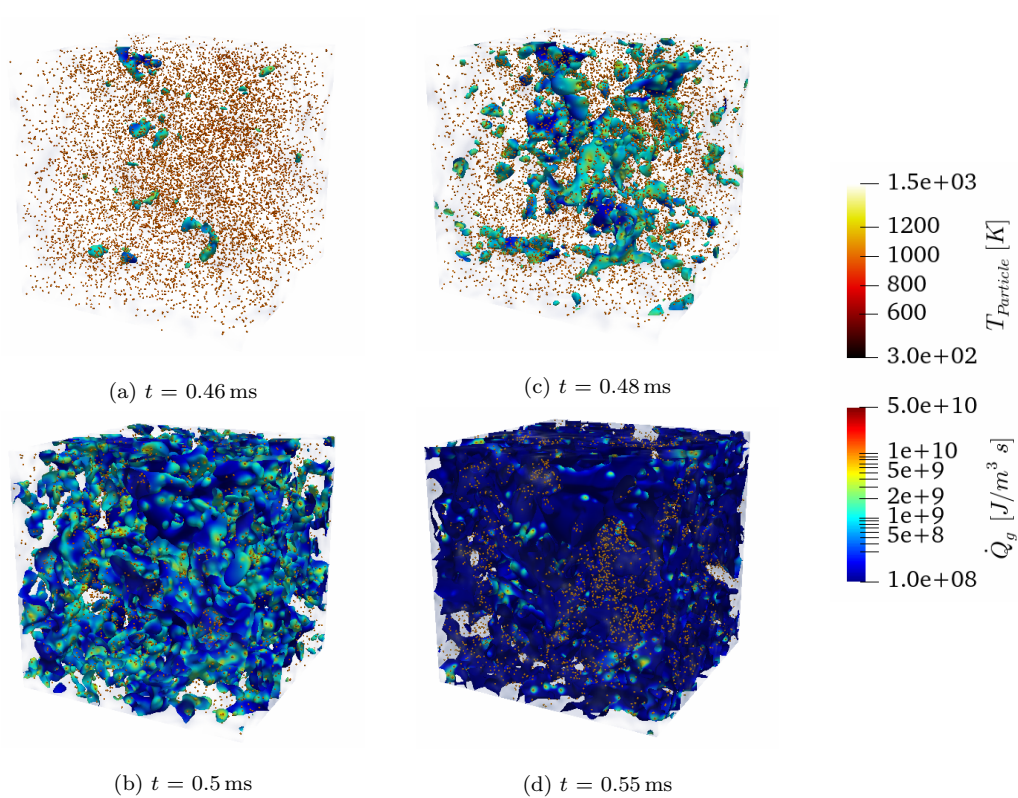


Fig. 2. Snapshots of the ignition process illustrated by the iso-surfaces of the 10% of the maximum OH mass fraction during the entire combustion process ( $Y_{\text{OH,max}}$ ) colored by heat release. Particles are shown with points colored by particle temperature.

330 are introduced to study the effect of particle clustering in the ignition and  
 331 combustion process. The ignition is investigated in each Voronoi region,  
 332 following the definition given in Section 2.4. When particle clusters form  
 333 in the turbulent field, the local particle number density increases at specific  
 334 volumes, and the local gas temperature decreases due to the energy sink  
 335 required for clustered particles heat-up at those locations. Therefore, the  
 336 thermo-chemical conditions are more suitable for ignition in the location  
 337 outside of the clusters, and as a result, the first ignition kernels are observed  
 338 mostly in those regions. This behavior is quantified in Fig. 3 with respect  
 339 to the normalized Voronoi volumes. Figure 3a shows the number of ignited  
 340 cells  $N_{\text{ign,cell}}$  normalized by the total number of cells in the numerical domain  
 341  $N_{\text{cell,tot}} = 256^3$ , where a higher number of ignited points can be observed  
 342 at volumes larger than  $V_C$ . Also, Fig. 3b shows an overall higher gas-phase  
 343 temperature at volumes larger than  $V_C$ . Recall that larger Voronoi volumes  
 344 indicate lower local particle number density, which is typically found outside  
 345 of particle clusters.

346 After investigating the position of the individually ignited regions, the  
 347 complete transient ignition process shown in Fig. 2 is quantified by calculat-  
 348 ing the number of the ignited regions and their corresponding volumes during  
 349 the ignition process. Fig. 4a shows an increase in the number of auto-ignited  
 350 regions from  $\tau_{\text{auto.ign}} \simeq 0.46$  ms until  $\tau_{\text{int.ign}} \simeq 0.5$  ms. At this point, no new  
 351 individual ignition kernels are formed. Subsequently, ignition kernels start  
 352 to merge, leading to a decrease in the number of separate ignited regions. Si-  
 353 multaneously, the total volume of the ignited regions starts to expand rapidly  
 354 due to flame propagation. This mode of ignition was recently introduced as

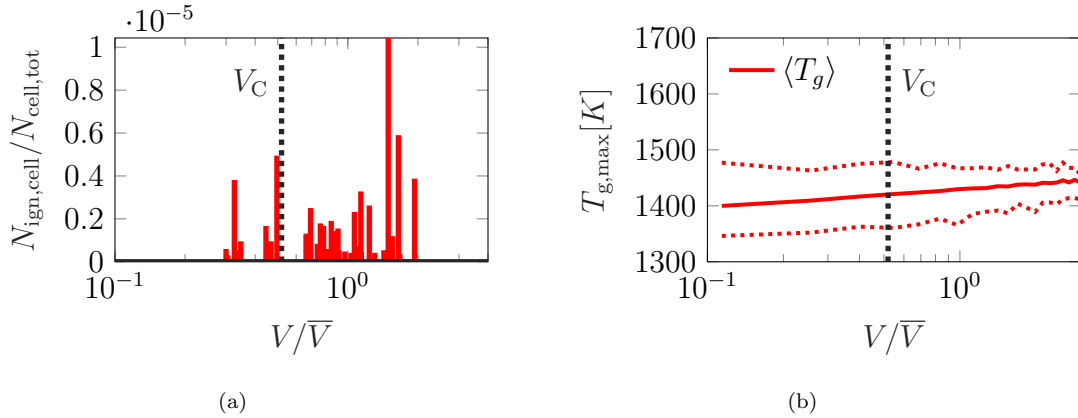


Fig. 3. a) Normalized number of the ignited cells and b) gas temperature in normalized Voronoi volumes at  $\tau_{\text{auto,ign}} \simeq 0.46$  ms. Red dotted lines show the minimum and maximum gas temperature in normalized Voronoi volumes. Volumes larger than  $V_C$  represent regions outside of clusters.

355 interaction ignition [58].

356 To compare the correlation between the ignition region and turbulent  
 357 scales, the Kolmogorov length ( $\eta$ ) is utilized as a reference length. Figure 4b  
 358 shows the PDF of the ignited region length scale  $l_{\text{ign}}$  normalized by the  
 359 Kolmogorov length for different instances of the ignition process. The ignited  
 360 region length scale is defined by assuming a spherical shape for the ignited  
 361 region  $l_{\text{ign}} = (6/\pi)V_{\text{ign}}^{1/3}$ . Ignition kernels with different sizes are indicated by  
 362 the broad PDF shape at  $t = 0.46$  ms and  $t = 0.5$  ms. After the ignition regions  
 363 merge ( $t > 0.5$  ms), the PDFs become narrower, suggesting that the regions  
 364 converge towards a certain size. According to the corresponding distributions  
 365 for  $t > 0.5$  ms, the PDF shows a weak bimodal behavior. The prominent peak  
 366 corresponds to the individual kernels and the large value of the PDF for large  
 367 ignition lengths corresponds to the merged kernels. Later in the ignition

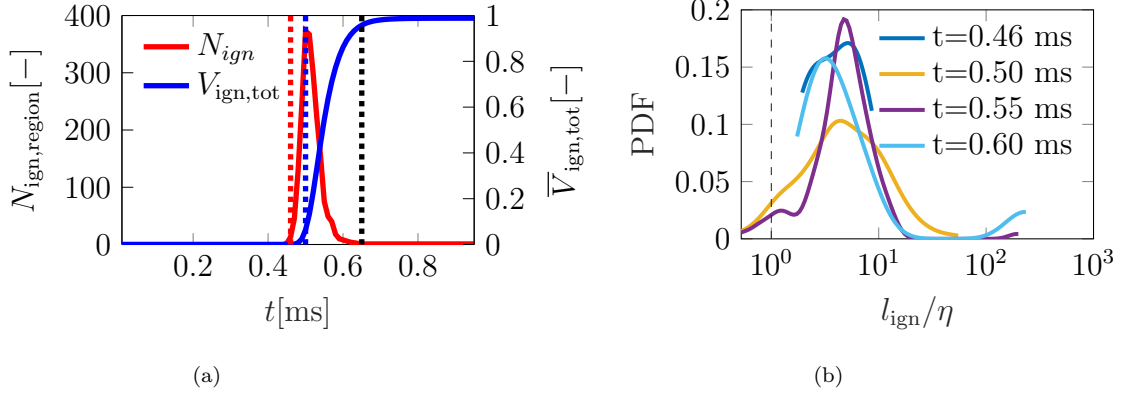


Fig. 4. a) Evolution of the number of separated ignited regions ( $N_{ign}$ ) and the total normalized volume  $\sum V_{ign}$  of the ignited regions. The vertical red, blue, and black dotted lines show the auto-ignition time, interaction ignition time, and end of the ignition process, respectively. b) Distribution of the ignited region length scale compared to the Kolmogorov scale  $\eta$ . The vertical dashed line corresponds to the Kolmogorov length scale.

368 process, the peak corresponding to the individual kernels shifts to smaller  
 369 ratios, and the PDF value in the far right grows, indicating an increase in  
 370 the number of merged kernels. An interesting observation is that the size  
 371 of the ignited regions consistently remains around one order of magnitude  
 372 larger than the Kolmogorov length scale. This is promoted due to the fact  
 373 that ignition happens primarily outside of the particle clusters, where a more  
 374 uniform volatile-oxidizer mixture with suitable thermo-chemical conditions  
 375 for ignition exists and can be ignited on larger length scales.

376 In order to study the suitable thermo-chemical conditions for ignition, the  
 377 mixture fraction and scalar dissipation rate concepts are utilized. Mixture  
 378 fraction indicates the amount of local volatile/oxidizer mixing and the scalar  
 379 dissipation rate represents the local rate of diffusive mixing at the molecu-

380 lar level, and therefore, it is a key element for the modeling of turbulence-  
 381 chemistry interaction. Figure 5 provides insights into the ignition conditions,  
 382 utilizing the scalar dissipation rate and mixture fraction calculated based on  
 383 Bilger’s definition, revealing that the ignition process primarily takes place in  
 384 lean mixtures ( $Z \sim 0.02$ ), specifically away from the particles. Considering  
 385 the fixed volatile composition assumption [5] for the released volatiles and  
 386 their global reaction with the oxidizer, the stoichiometric mixture fraction  
 387 is  $Z_{st} = 0.117$ . This observation aligns with the findings from the Voronoi  
 388 analysis. Larger Voronoi volumes indicate locations outside of a cluster that  
 389 leads to lower released volatiles and, as a result, a lower amount of fuel in  
 390 ignited regions. Additionally, Fig. 5a shows that at  $\tau_{\text{auto.ign}} \simeq 0.46$  ms, some  
 391 locations in the domain, characterized by the same mixture fractions, do not  
 392 undergo ignition. Notably, for a given mixture fraction, regions with smaller  
 393 scalar dissipation rate ignite first.

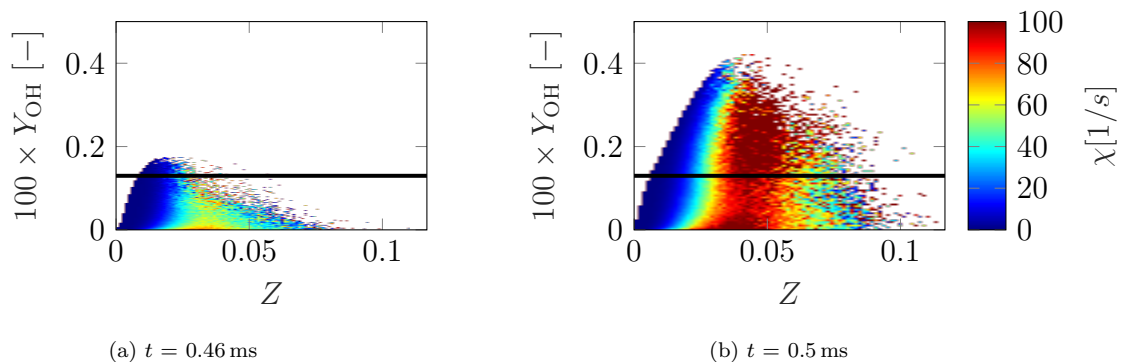


Fig. 5. OH mass fraction and mixture fraction colored by the scalar dissipation at  $t = 0.46$  ms and  $t = 0.5$  ms. The horizontal black line shows the ignition threshold for OH mass fraction based on the ignition definition.

394 As shown in Fig. 5b, at later times during ignition ( $\tau_{\text{int.ign}} \simeq 0.5$  ms), lo-

395 cations with higher scalar dissipation rates also ignite at higher mixture frac-  
 396 tions, which are closer to the clusters, where volatiles are released. Also, high  
 397 scalar dissipation rates near the clusters (higher mixture fractions) promote  
 398 mixing, leading to a premixed mixture of volatiles and the oxidizer, which  
 399 facilitates premixed flame propagation from the ignited regions toward the  
 400 clusters.

401 The particle clouds ignition process is inherently transient, and the pres-  
 402 ence of particle clustering further affects the reactivity [31]. Therefore, it is  
 403 crucial to carefully evaluate the assumptions made in reduced-order models  
 404 for ignition and combustion to predict important flame characteristics in this  
 405 particular configuration.

406 *4.2. A priori model assessment of clustering particle clouds in the prediction*  
 407 *of the ignition process*

408 In this section, a systematic assessment based on error decomposition is  
 409 used to evaluate the overall performance of the model from different perspec-  
 410 tives. First, the performance of the tabulated chemistry in a flamelet/progress  
 411 variable (FPV) model compared to DNS is studied to quantify the suitability  
 412 of the tabulated thermo-chemical state. Second, the presumed PDF used to  
 413 pre-integrate the table is compared with the filtered DNS dataset to find the  
 414 optimal presumed PDF shapes for each input parameter of the table.

415 The reference progress variable is defined as [4]

$$C_{\text{ref}} = \frac{Y_{\text{CO}_2}}{\mathcal{M}_{\text{CO}_2}} + \frac{Y_{\text{CO}}}{\mathcal{M}_{\text{CO}}} - \frac{Y_{\text{O}_2}}{\mathcal{M}_{\text{O}_2}}, \quad (9)$$

416 where  $\mathcal{M}_i$  is the molar mass of species  $i$ .

417 The total modeling errors are systematically decomposed into the func-  
418 tional and irreducible errors employing the optimal estimator method de-  
419 scribed in Section 2.3.

#### 420 4.2.1. Assessment of the thermo-chemical states in tabulated chemistry

421 In order to have a general overview of the FPV model performance, the  
422 volume-averaged  $\langle T_g \rangle$  and  $\langle \dot{\omega}_C \rangle$  in the entire domain at different times during  
423 ignition and combustion are calculated, according to the model described  
424 in Section 2.2 and compared with the DNS data. To calculate a volume-  
425 averaged quantity  $\langle \phi \rangle$  in the DNS and the FPV model, the following equation  
426 is used

$$\langle \phi(t) \rangle = \frac{1}{N} \sum_{i=1}^N (\phi_i(t)), \quad (10)$$

427 where  $N$  is the total number of cells in the entire volume. As illustrated in  
428 Fig. 6, the comparison between the model and reference data shows good  
429 overall agreement in gas temperature, although increased deviations are ap-  
430 parent for later times. Comparing the progress variable source term shows  
431 a shift in the prediction of the FPV model compared to the DNS, which  
432 indicates later ignition delay time prediction by the model. However, nearly  
433 the same peak average value of the progress variable source term is observed  
434 in the FPV model. In order to investigate the differences during the igni-  
435 tion process, the progress variable source term ( $\dot{\omega}_C$ ) is chosen as the quantity  
436 of interest for modeling particle cloud ignition and combustion processes in  
437 isotropic turbulence.

438 To understand the origin of the deviations in the FPV model from the  
439 DNS results, the performance of the model inside and outside of the particle



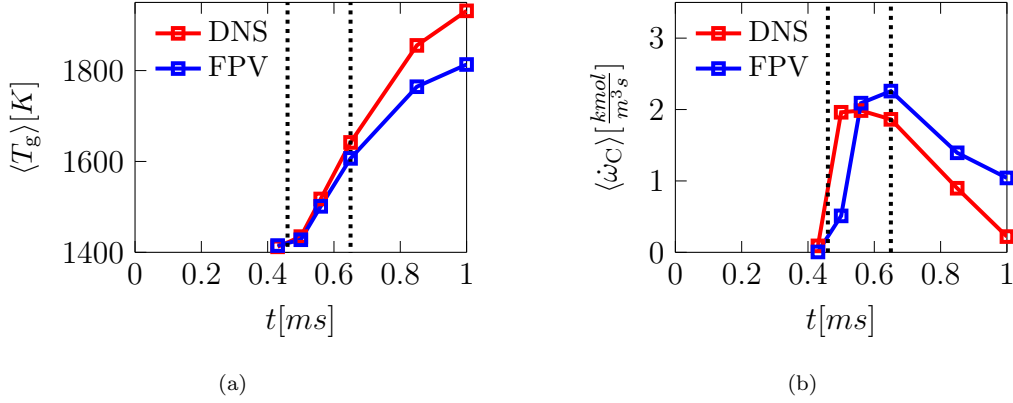


Fig. 6. Overall comparison between the DNS data and the FPV model in predicting the volume-averaged a) gas temperature, and b) progress variable source term at different times. Vertical dotted lines indicate the start and end of the ignition process based on Fig. 4a.

440 clusters is studied in more detail. To this end, two different time instances,  
 441  $t = 0.5$  ms with the maximum number of ignited regions during the ignition  
 442 process and  $t = 0.65$  ms, which is at the end of the ignition process, as shown  
 443 in Fig. 4a, are chosen. First, the model parameters chosen to parameter-  
 444 ize the flamelet table are assessed by the optimal estimator method. This  
 445 enables calculating the irreducible errors for different sets of input parame-  
 446 ters for predicting the quantity of interest. To obtain a meaningful value for  
 447 the errors with respect to particle cluster locations, they are normalized by  
 448 the maximum value of the conditionally averaged quantity of interest in the  
 449 normalized Voronoi volumes ( $V/\bar{V}$ ).

$$\bar{\epsilon} = \frac{\sqrt{\epsilon^2}}{\max(\langle Q_{int} | V/\bar{V} \rangle)}. \quad (11)$$

450 Different combinations of mixture fraction, progress variable, and enthalpy,  
 451 as well as the OH mass fraction, as it is one of the most important ignition

452 identifier species, are used to find the best possible set of parameters to  
 453 characterize the composition space.

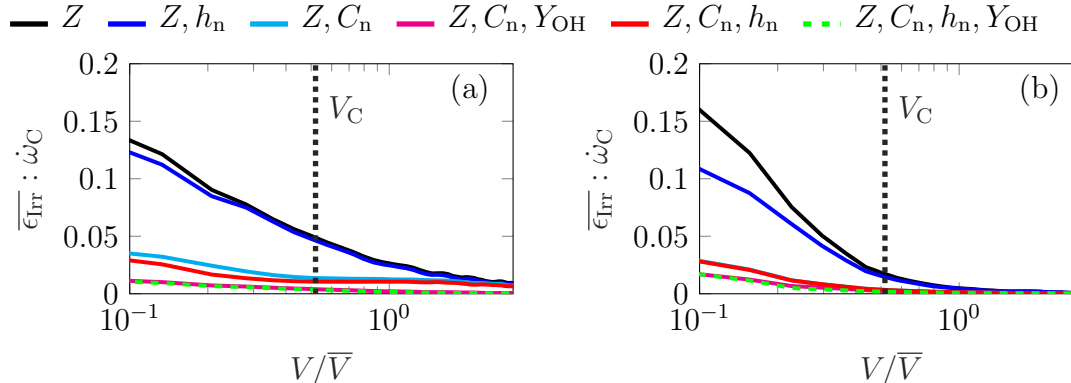


Fig. 7. Irreducible errors of different input parameters in predicting progress variable source term at a)  $t = 0.5$  ms and b)  $t = 0.65$  ms. Volumes larger than  $V_C$  represent regions outside of clusters.

454 After comparing the different combinations, Fig. 7 demonstrates that  
 455 the inclusion of the progress variable and enthalpy alongside the mixture  
 456 fraction strongly decreases the overall irreducible error, especially inside the  
 457 clusters at early times, where the errors are highest. It is interesting also  
 458 to note that consideration of enthalpy is not needed if only the chemical  
 459 source term is of interest. Including  $Y_{OH}$  as an input parameter leads to  
 460 a slight improvement in the overall irreducible error. However, the error  
 461 corresponding to  $Z, C_n, Y_{OH}$  is still comparable with the error corresponding  
 462 to  $Z, C_n$  and  $Z, C_n, h_n$ . Also, creating a table with OH radical, which can  
 463 perform well in the *a posteriori* LES, is very challenging, since OH radical  
 464 is not readily available in LES. As a result, in this study, this radical is not  
 465 considered as an additional input parameter.

466 Next, the functional errors are assessed at  $t = 0.5$  ms and  $t = 0.65$  ms.  
 467 Using the parameters  $Z$ ,  $h_n$ , and  $C_n$ , as discussed earlier, a flamelet table  
 468 is generated. The quantity of interest from the table are compared with  
 469 the corresponding values from the DNS datasets to calculate the functional  
 470 errors based on equation (5) and (6).

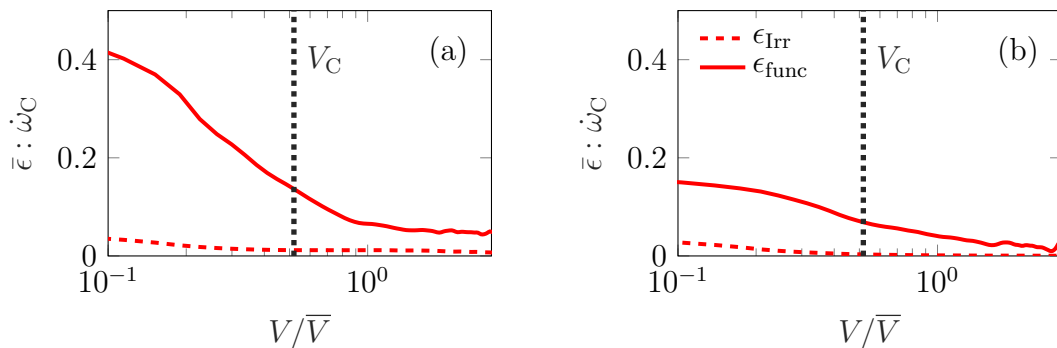


Fig. 8. Errors involved in the reference FPV model in comparison with the DNS results in the prediction of progress variable source term at a)  $t = 0.5$  ms and b)  $t = 0.65$  ms. Volumes larger than  $V_C$  represent regions outside of clusters.

471 Figure 8 compares the progress variable source term between the flamelet  
 472 table and the DNS. The tabulated flamelet model exhibits certain limitations  
 473 in accurately predicting  $\dot{\omega}_C$ , particularly within the particle clusters.

474 Comparing the model performance at two different time instances shows  
 475 that for  $\dot{\omega}_C$  the modeling error is higher at ignition. The increased functional  
 476 error observed during the ignition process primarily occurs within the particle  
 477 clusters, specifically in close proximity to the particles themselves. This  
 478 can be attributed to the limitations of the typically used flamelet tables in  
 479 capturing the particle-chemistry interactions due to the fact that the particle  
 480 effects in the flamelet table are not considered. This limitation is especially

481 prominent in the vicinity of particle clusters, which corresponds to a smaller  
 482 mixing time scale compared to the chemical time scale. In these regions,  
 483 where the volatiles mix with the oxidizer prior to ignition, the flame behavior  
 484 resembles that of a premixed flame, which cannot be accurately captured by  
 485 the non-premixed flamelet approach employed in this study.

486 After assessing the reference FPV model’s input parameters and its per-  
 487 formance in predicting the quantity of interest, the effects of changing the  
 488 input parameters, such as excluding enthalpy and altering the progress vari-  
 489 able definition in the model performance, are examined next.

#### 490 4.2.2. Effect of heat losses in flamelet tabulation

491 In order to investigate the effect of heat losses in the table, a table with  
 492 two input parameters ( $Z$  and  $C_n$ ) is generated. Its performance is compared  
 493 with the reference FPV model ( $Z$ ,  $C_n$ , and  $h_n$ ). From Fig. 9, it is evident  
 494 that including enthalpy in the table primarily affects the predictions.

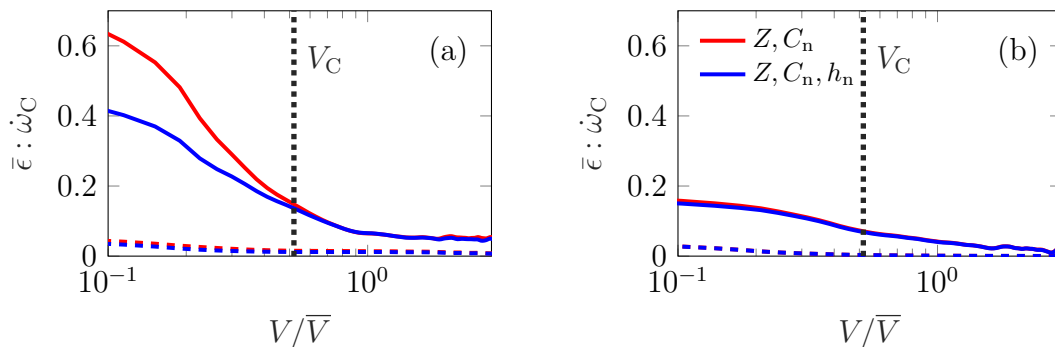


Fig. 9. Effect of enthalpy in the errors of progress variable source term at a)  $t = 0.5$  ms and b)  $t = 0.65$  ms. Solid color lines show the functional errors and dashed color lines are the corresponding irreducible errors. Volumes larger than  $V_C$  represent regions outside of clusters.

495 The results demonstrate that incorporating enthalpy as an input param-  
 496 eter improves the accuracy inside the clusters, particularly during ignition.  
 497 This suggests that the ignition phase is more sensitive to changes in enthalpy  
 498 compared to later stages of combustion, especially inside the clusters. During  
 499 the ignition phase, due to the particle heat-up process and the higher tem-  
 500 perature gradients between particles and the gas phase, the heat loss effect  
 501 is more dominant than at later times [16].

#### 502 4.2.3. Effect of progress variable definition

503 In this section, the effect of altering the progress variables definition on  
 504 model performance is investigated. To this end, three different progress vari-  
 505 ables, as defined in Table 1, are compared with the reference definition ( $\mathcal{C}_{\text{ref}}$ )  
 506 in equation (9). These definitions are employed to compare the typically  
 507 used definitions in flamelet tabulated chemistry models [4, 7] for pulverized  
 508 solid fuel combustion and to investigate the effect of removing certain species  
 509 from the progress variable definition.

Table 1: Different progress variable definitions

$\mathcal{C}$	Definition
$\mathcal{C}_1$	$Y_{\text{CO}_2} + Y_{\text{CO}}$
$\mathcal{C}_2$	$Y_{\text{CO}_2} - Y_{\text{O}_2}$
$\mathcal{C}_3$	$Y_{\text{CO}_2}/\mathcal{M}_{\text{CO}_2} + Y_{\text{H}_2\text{O}}/\mathcal{M}_{\text{H}_2\text{O}} - Y_{\text{O}_2}/\mathcal{M}_{\text{O}_2}$

510 Figure 10 shows the effect of progress variable definition on the overall  
 511 model performance. It can be observed that excluding CO or O<sub>2</sub> from the  
 512 model significantly amplifies the functional errors of predicting the progress

513 variable source term ( $\dot{\omega}_C$ ), indicating that  $\mathcal{C}_1$  and  $\mathcal{C}_2$  are not suitable choices  
 514 for representing the progress variable. On the other hand, replacing CO with  
 515 H<sub>2</sub>O ( $\mathcal{C}_3$ ) resulted in an improvement in predicting the quantity of interest,  
 516 particularly within the clusters.

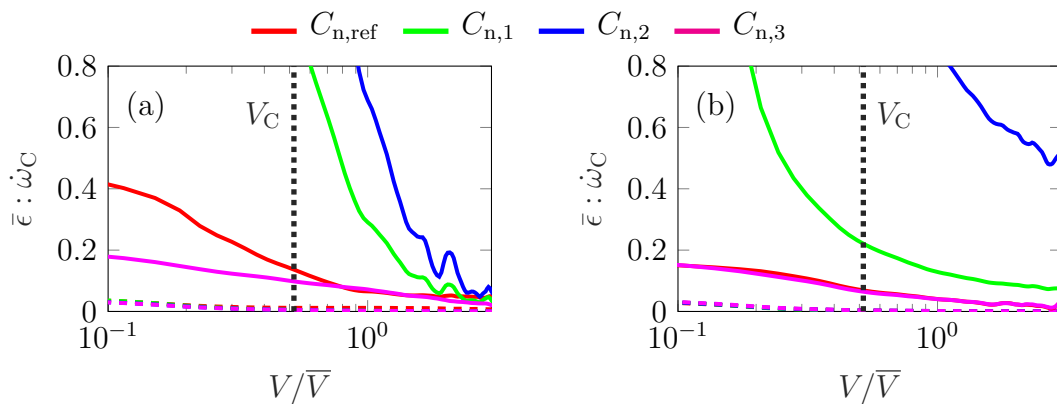


Fig. 10. Effect of progress variable definition in the errors of progress variable source term at a)  $t = 0.5$  ms and b)  $t = 0.65$  ms. Solid color lines show the functional errors and dashed color lines are the corresponding irreducible errors. Volumes larger than  $V_C$  represent regions outside of clusters.

517 *4.2.4. Assessment of the presumed PDF shapes in comparison with subgrid*  
 518 *scalar PDF*

519 In the context of LES, only filtered scalars are transported, which cannot  
 520 be used directly for table access. The unresolved subgrid distribution of the  
 521 transported scalars is often modeled by a presumed- $\beta$  PDF for the mixture  
 522 fraction  $Z$ , whereas the distributions of the remaining scalars are modeled by  
 523 a  $\delta$  function [1, 14]. These assumptions will be examined in the following by  
 524 employing different presumed PDF shapes for the table input parameters.  
 525 By comparing the results to the DNS data, the suitability of considering

526 subgrid-scale fluctuations can be analyzed.

527 In order to evaluate the model performance when coupled to LES, the  
528 DNS dataset is filtered using a box filter of width  $\Delta_f = 8\Delta x$ , ensuring  
529 an averaged resolved energy of about 90% with respect to the DNS field,  
530 which is a typical value for a well-resolved LES [59]. After filtering, the  
531 distribution of the input parameters ( $Z$ ,  $h_n$ ,  $C_n$ ) from the DNS is examined to  
532 determine suitable PDF shapes that accurately represent the behavior of each  
533 input parameter. In Fig. 11, various PDF shapes ( $\delta$ ,  $\beta$ , and Top-hat (TH)  
534 distributions), which are widely used in the pulverized solid fuel modeling [4,  
535 6, 22, 47], based on the Favre-averaged mean and variance of the filtered  
536 dataset are compared with the distribution of the input parameters obtained  
537 from the DNS dataset at two different time instances within a specific filter  
538 cell of the DNS field.

539 It should be noted that in the context of point-particle DNS, distribut-  
540 ing the particles' source term over a specific kernel shape can impact the  
541 evolution of the mixture fraction PDF. Distributing the source term across  
542 a Gaussian kernel, a technique applied to better account for finite size ef-  
543 fects of particles [32, 38, 60] results in a broader source term distribution,  
544 diminishing peak values on the fuel side. Consequently, both the mean and  
545 variance of the mixture fraction decrease, affecting the PDF shape. How-  
546 ever, it is expected that the overall shape of the PDF remains similar, and  
547 only the width of the distribution would be affected by the distribution of  
548 the source term compared to fully resolved simulations, which incorporate  
549 particle boundary layer effects. Incorporating boundary layer effects into the  
550 present study, as evidenced by Wang et al. [61], would complicate the model

551 assessment procedure and require further investigation using fully resolved  
 552 simulations. However, considering the finite-size particle effects ensures a  
 553 more realistic benchmark for the subgrid scalar PDF assessment.

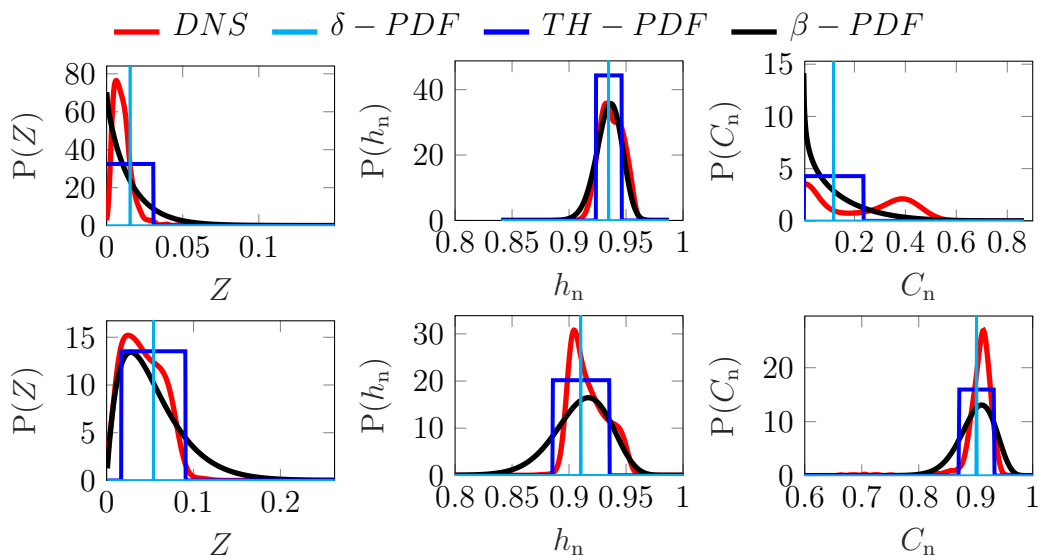


Fig. 11. Comparing different presumed PDF shapes for mixture fraction, normalized enthalpy, and normalized progress variable with subgrid scalar PDF in an example DNS filter cell at  $t = 0.5$  ms (top row) and  $t = 0.65$  ms (bottom row).

554 Comparing different presumed PDF shapes based on Fig. 11 shows that  
 555 all presumed approaches have difficulties in approximating the DNS distribu-  
 556 tion. Top-hat distributions are symmetrical with respect to the mean and, as  
 557 a result, cannot capture the non-symmetrical DNS, which is originated from  
 558 the particle clustering effects. Mixture fraction distribution shows higher  
 559 probabilities in smaller mixture fractions, which is due to more data points  
 560 outside of clusters. It can also be observed that for the mixture fraction, as  
 561 suggested in the original formulation for single-phase combustion [42], the  
 562  $\beta$  distribution yields a more accurate distribution than other PDF shapes



563 compared to the DNS for clustering particle cloud ignition.

564 To complement the qualitative investigation of the presumed PDF shapes  
 565 shown in Fig. 11, the errors involved in the model when using presumed PDF  
 566 assumption during clustering particle cloud ignition and combustion is eval-  
 567 uated. Since the selected PDF shapes can be represented by the first two  
 568 moments, meaning mean and variance, incorporating different PDF shapes  
 569 for mixture fraction, progress variable, and enthalpy would require their mean  
 570 and variance as inputs of the model. It should be noted that utilizing higher-  
 571 order moments can lead to a more accurate representation of the DNS distri-  
 572 bution. However, this can lead to a further increase in the table dimensions.  
 573 In order to determine the optimal input sets, including the variances, the  
 574 concept of optimal estimator is employed to calculate the irreducible error  
 575 associated with each set.

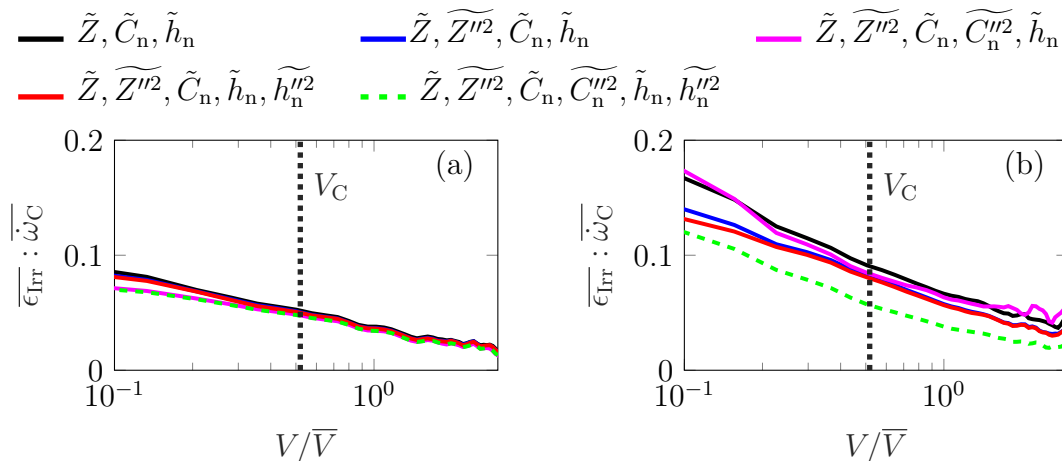


Fig. 12. Effect of adding the variance of different input parameters in the irreducible error of filtered progress variable source term at a)  $t = 0.5$  ms and b)  $t = 0.65$  ms. Volumes larger than  $V_C$  represent regions outside a cluster.

576 Figure 12 shows the irreducible error for predicting the filtered progress  
577 variable source term using different sets of input parameters, including vari-  
578 ances. It can be observed that at ignition, adding the variances to the ref-  
579 erence Favre-averaged input set  $(\tilde{Z}, \tilde{C}_n, \tilde{h}_n)$  does not improve the results  
580 very much. This shows that the model is not sensitive to variances of input  
581 parameters at ignition. The mixture fraction distribution in Fig. 11 shows  
582 a smaller variance during ignition compared to the end of ignition due to a  
583 lower total volatile release. Also, considering variances of progress variables  
584 and enthalpy is not sufficient for the correct prediction of the quantity of  
585 interest in the filter cells at ignition.

586 It should be mentioned that at  $t = 0.65$  ms, adding variances to the  
587 reference input set improves the irreducible error. This improvement in the  
588 prediction is due to the larger variances (especially  $\widetilde{Z''^2}$ ) and non-linearity  
589 of the progress variable source term with respect to input parameters in the  
590 filter cells.

591 After analyzing different input parameter sets and studying the effect of  
592 PDF shape on irreducible error, it is necessary to investigate the impact of  
593 including variances in the functional errors for predicting the filtered quantity  
594 of interest. The non-symmetrical characteristic of the DNS distribution due  
595 to particle clustering can be better represented by a  $\beta$ -PDF. Therefore, this  
596 study focuses on investigating the performance of using  $\beta$ -PDF in comparison  
597 with a  $\delta$  function and the filtered model results. The  $\delta$  function corresponds  
598 to not considering the sub-filter distributions in the model, and the filtered  
599 model inherently considers the correct sub-filter joint distributions of the  
600 DNS data without the assumption of presumed PDF shapes.

601 To this end, four different combinations of PDF shapes, as shown in  
 602 Fig. 13, are applied. First, a  $\delta$  function for all input scalars ( $3\delta$ ) is assumed.  
 603 Then the typical assumption of a  $\beta$  distribution for mixture fraction while  
 604 maintaining a  $\delta$  function for progress variable and enthalpy ( $1\beta$ ) serves as  
 605 the reference model. In addition, the performance of the model is evaluated  
 606 by employing  $\beta$  distribution for mixture fraction and progress variable ( $2\beta$ ).  
 607 Finally, a  $\beta$  distribution for all input parameters ( $3\beta$ ) is investigated.

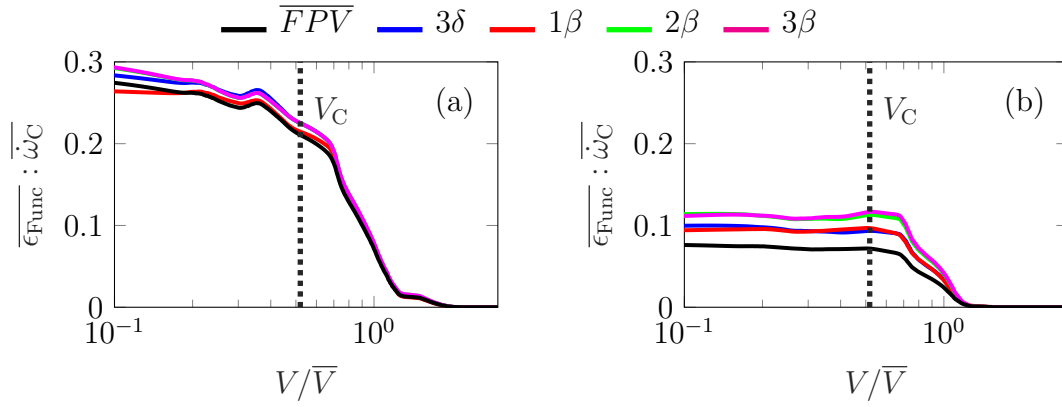


Fig. 13. Functional errors of filtered progress variable source term at a)  $t = 0.5$  ms and  
 b)  $t = 0.65$  ms for different PDF assumptions in the FPV model. Volumes larger than  $V_C$   
 represent regions outside of clusters.

608 Figure 13 shows the normalized functional errors for  $\overline{\omega_C}$ . These errors are  
 609 calculated based on equations (4), (5), (6), and (11). The functional error for  
 610 each PDF combination is compared with the respective error for the filtered  
 611 FPV model results, which inherently considers the correct sub-filter joint  
 612 distributions of the DNS data.

613 Around the ignition phase ( $t = 0.5$  ms), all of the investigated PDF  
 614 shapes exhibit comparable performance to the filtered FPV model results

615 in predicting  $\overline{\dot{\omega}_C}$ . This finding aligns with the results from Fig. 12, which  
616 indicate that including variances as additional input parameters does not  
617 improve the errors. Hence, using the  $\delta$  function as PDF shape for all input  
618 parameters can capture the ignition process as well as other models. This  
619 indicates that the distribution of sub-filters does not significantly affect the  
620 prediction of the progress variable source term during ignition, and the main  
621 contribution to the total modeling error is due to the performance of the  
622 non-premixed flamelet table.

623 However, towards the end of the ignition phase ( $t = 0.65$  ms), the mixture  
624 fraction in the subgrid has a larger variance compared to the time of ignition.  
625 Consequently, it has a more pronounced influence on the PDF shapes, par-  
626 ticularly within the particle clusters, as shown in Fig. 11. In these regions,  
627 the reference model  $1\beta$  shows a better overall performance in predicting  $\overline{\dot{\omega}_C}$ .  
628 However,  $2\beta$  and  $3\beta$  models show worse predictions, which shows that choos-  
629 ing the  $\beta$  distributions for progress variable and enthalpy is not a good choice  
630 for predicting the quantity of interest in clustering particle cloud combustion.

631 The performance of different presumed PDF assumptions in predicting  
632 the quantity of interest is further analyzed in Fig. 14. Here, the prediction  
633 of  $\overline{\dot{\omega}_C}$  using three models  $3\delta$ ,  $1\beta$ , and  $3\beta$  is compared with the filtered FPV  
634 predictions.

635 This comparison is chosen to provide further insight into the effect of  
636 including input parameter distributions in the final prediction of the quantity  
637 of interest. Similar to the results from Fig. 13, Fig. 14 show that around  
638 ignition, all presumed PDF shapes show the same performance. However,  
639 at the end of the ignition process ( $t = 0.65$  ms), using the  $3\delta$  and  $3\beta$  model

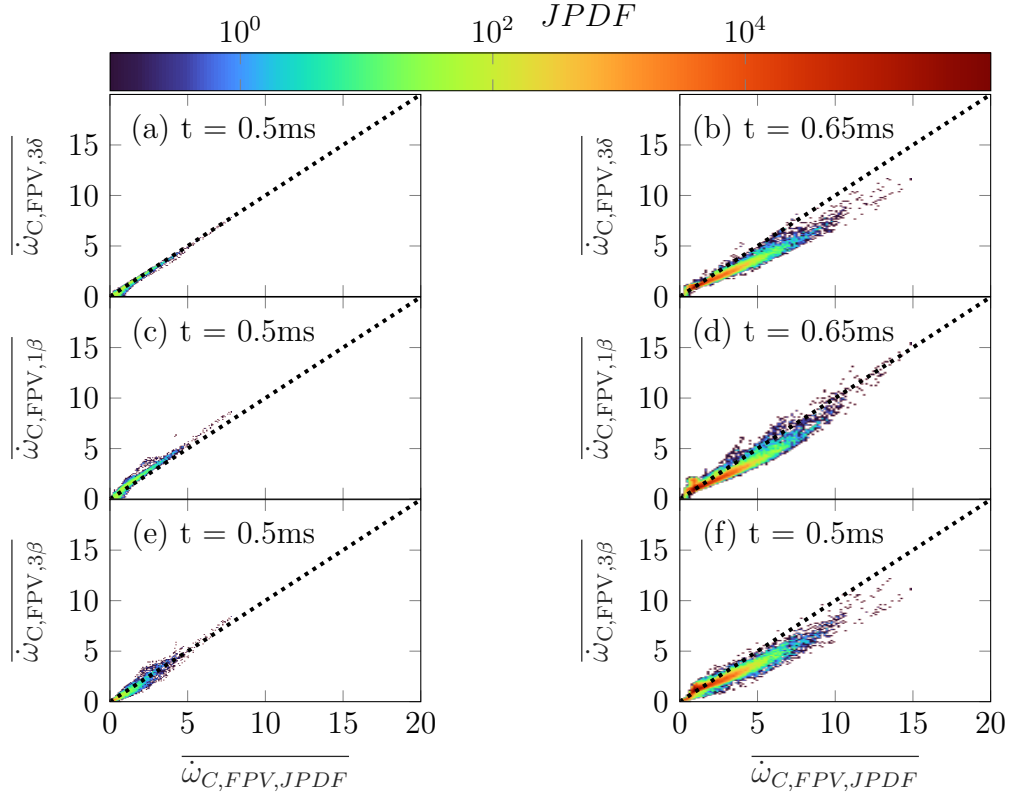


Fig. 14. Comparison between different PDF assumptions in the FPV model ( $3\delta = \delta(\tilde{Z})\delta(\tilde{C})\delta(\tilde{h})$ ,  $1\beta = \beta(\tilde{Z})$ , and  $3\beta = \beta(\tilde{Z})\beta(\tilde{C})\beta(\tilde{h})$ ) and the filtered-FPV prediction for progress variable source term ( $\overline{\dot{\omega}_{C,FPV,JPDF}}$ ) at  $t = 0.5$  ms and  $t = 0.65$  ms

640 can lead to worse predictions compared to  $1/\beta$  model for higher progress  
641 variable source terms. This is due to incorrectly assumed PDF shapes at  
642 these conditions.

## 643 **5. Conclusions**

644 This study presents a comprehensive investigation of modeling the homo-  
645 geneous ignition in clustering particle clouds in isotropic turbulence. For this  
646 purpose, a DNS of pulverized coal particles using the point-particle model  
647 for the dispersed phase and detailed chemical kinetics for the gas phase was  
648 performed.

649 Initially, auto-ignition was found at positions with favorable thermo-  
650 chemical states, followed by growing and merging the individual ignition  
651 kernels. It was observed that particle clustering has a significant impact on  
652 the ignition process. Ignition predominantly occurs in regions outside of the  
653 clusters, where higher temperatures are present due to reduced energy sink  
654 associated with particle heating. These ignition locations exhibit a lean mix-  
655 ture of released volatiles and oxidizer, resulting in lower scalar dissipation  
656 compared to the cluster locations.

657 This study employed a systematic error decomposition approach, utilizing  
658 the optimal estimator concept, to assess tabulated flamelet models in parti-  
659 cle clustering conditions. The assessment focused on determining the errors  
660 associated with the reference flamelet/progress variable (FPV) model inputs  
661 and evaluating its functional model performance both inside and outside of  
662 particle clusters. The assessment of the FPV model revealed its good perfor-  
663 mance in predicting the progress variable source term. However, around the

664 ignition phase, a higher deviation from the prediction by the DNS data was  
665 observed, particularly for the progress variable source term inside particle  
666 clusters. This study identified an efficient set of input parameters that yields  
667 the smallest irreducible errors, consisting of mixture fraction  $Z$ , normalized  
668 progress variable  $C_n$ , and enthalpy  $hn$ . Not including the enthalpy resulted in  
669 higher errors, especially during the ignition phase, highlighting the increased  
670 sensitivity of quantity of interest to enthalpy in the ignition phase. Regard-  
671 ing the progress variable definition, it was found that including  $\text{CO}_2$ ,  $\text{CO}$ ,  
672 and  $\text{O}_2$  as the set of parameters showed good performance in predicting the  
673 quantity of interest. Omitting either  $\text{CO}$  or  $\text{O}_2$  led to a significant increase  
674 in functional modeling errors when predicting the progress variable source  
675 term. Also, replacing  $\text{CO}$  with  $\text{H}_2\text{O}$  improved the prediction of the progress  
676 variable source term during the ignition phase, especially inside the clusters.

677 The findings reveal that incorporating the variances of the input param-  
678 eters improves the irreducible errors, especially inside particle clusters, pri-  
679 marily at the end of the ignition process, where the sub-filter distribution  
680 of the DNS data exhibits larger variances. In contrast, during the ignition  
681 onset, when individual kernels with small variances dominate due to particle  
682 clustering effects on ignition location, a  $\delta$  function shows a good performance.  
683 However, in the case of functional errors, the presumed marginal PDF shape  
684 assumption is prone to errors originating from the shape function. Choosing  
685 the correct presumed PDF shape that matches the DNS sub-filter distribu-  
686 tion is challenging and has an important impact on the model's performance.

687 **Acknowledgments**

688 The authors kindly acknowledge financial support through Deutsche For-  
 689 schungsgemeinschaft (DFG) Projektnummer 215035359 - through SFB/TRR  
 690 129. The authors also gratefully acknowledge the computing time provided to  
 691 them at the NHR Center NHR4CES at RWTH Aachen University (project  
 692 number p0020514 and p0021020). This is funded by the Federal Ministry  
 693 of Education and Research, and the state governments participating on the  
 694 basis of the resolutions of the GWK for national high performance computing  
 695 at universities.

696 **Appendix A**

697 The turbulence statistics for the studied isotropic turbulence configura-  
 698 tion during different time instances are briefly summarized in table 2.

Table 2: Turbulence statistics at different time instances

time [ms]	$Re_\lambda$	$Re_{Turb}$	$\eta[m]$	$l_t[m]$	$t_\eta[ms]$	$t_l[ms]$	$St$
0	30.7	141.8	1.04E-04	4.27E-03	4.47E-02	5.33E-01	6.199
0.46	30.9	143.9	9.94E-05	4.13E-03	4.16E-02	4.99E-01	6.207
0.5	30.5	140.1	9.96E-05	4.06E-03	4.27E-02	5.05E-01	6.333
0.55	29.4	129.8	1.01E-04	3.88E-03	4.34E-02	4.94E-01	6.032
0.6	28.5	122.1	1.02E-04	3.76E-03	4.46E-02	4.92E-01	5.775
0.65	27.7	115.2	1.04E-04	3.66E-03	4.48E-02	4.81E-01	5.365

699  $\eta$  and  $t_\eta$  are the respective Kolmogorov length and time scales, and  $l_t$  and  $t_l$   
 700 correspond to integral length and time scales.



701 **References**

- 702 [1] C. Hasse, P. Debiagi, X. Wen, K. Hildebrandt, M. Vascellari, T. Far-  
703 avelli, Advanced modeling approaches for CFD simulations of coal com-  
704 bustion and gasification, *Progress in Energy and Combustion Science* 86  
705 (2021) 100938.
- 706 [2] T. H. Fletcher, A. R. Kerstein, R. J. Pugmire, D. M. Grant, Chemical  
707 percolation model for devolatilization. 2. temperature and heating rate  
708 effects on product yields, *Energy & Fuels* 4 (1990) 54–60.
- 709 [3] T. Maffei, R. Khatami, S. Pierucci, T. Faravelli, E. Ranzi, Y. A. Lev-  
710 endis, Experimental and modeling study of single coal particle combus-  
711 tion in  $O_2/N_2$  and oxy-fuel ( $O_2/CO_2$ ) atmospheres, *Combustion and*  
712 *Flame* 160 (2013) 2559–2572.
- 713 [4] H. Nicolai, P. Debiagi, X. Wen, L. Dressler, A. Massmeyer, J. Janicka,  
714 C. Hasse, Flamelet LES of swirl-stabilized oxy-fuel flames using directly  
715 coupled multi-step solid fuel kinetics, *Combustion and Flame* 241 (2022)  
716 112062.
- 717 [5] P. Farmand, H. Nicolai, C. Schumann, A. Attili, L. Berger, T. Li, C.  
718 Geschwindner, F. di Mare, C. Hasse, B. Böhm, et al., Numerical inves-  
719 tigation and assessment of flamelet-based models for the prediction of  
720 pulverized solid fuel homogeneous ignition and combustion, *Combustion*  
721 *and Flame* 235 (2022) 111693.
- 722 [6] M. Rieth, A. Clements, M. Rabaçal, F. Proch, O. Stein, A. Kempf,  
723 Flamelet LES modeling of coal combustion with detailed devolatilization

- 724 by directly coupled CPD, Proceedings of the Combustion Institute 36  
725 (2017) 2181–2189.
- 726 [7] H. Nicolai, P. Debiagi, J. Janicka, C. Hasse, Flamelet LES of oxy-  
727 fuel swirling flames with different  $O_2/CO_2$  ratios using directly coupled  
728 seamless multi-step solid fuel kinetics, Fuel 344 (2023) 128089.
- 729 [8] T. H. Fletcher, Review of 30 years of research using the chemical perco-  
730 lation devolatilization model, Energy & Fuels 33 (2019) 12123–12153.
- 731 [9] C. Yin, J. Yan, Oxy-fuel combustion of pulverized fuels: Combustion  
732 fundamentals and modeling, Applied Energy 162 (2016) 742–762.
- 733 [10] O. Stein, G. Olenik, A. Kronenburg, F. Cavallo Marincola, B. Franchetti,  
734 A. Kempf, M. Ghiani, M. Vascellari, C. Hasse, Towards comprehensive  
735 coal combustion modelling for LES, Flow, turbulence and combustion  
736 90 (2013) 859–884.
- 737 [11] H. Nicolai, X. Wen, F. Miranda, D. Zabrodiec, A. Massmeyer, F.  
738 Di Mare, A. Dreizler, C. Hasse, R. Kneer, J. Janicka, Numerical in-  
739 vestigation of swirl-stabilized pulverized coal flames in air and oxy-fuel  
740 atmospheres by means of large eddy simulation coupled with tabulated  
741 chemistry, Fuel 287 (2021) 119429.
- 742 [12] H. Nicolai, G. Kuenne, R. Knappstein, H. Schneider, L. Becker, C.  
743 Hasse, F. di Mare, A. Dreizler, J. Janicka, Large eddy simulation of  
744 a laboratory-scale gas-assisted pulverized coal combustion chamber un-  
745 der oxy-fuel atmospheres using tabulated chemistry, Fuel 272 (2020)  
746 117683.

- 747 [13] X. Wen, H. Nicolai, H. Schneider, L. Cai, J. Janicka, H. Pitsch, C. Hasse,  
748 Flamelet LES of a swirl-stabilized multi-stream pulverized coal burner  
749 in air and oxy-fuel atmospheres with pollutant formation, Proceedings  
750 of the Combustion Institute 38 (2021) 4141–4149.
- 751 [14] M. Rieth, F. Proch, M. Rabaçal, B. Franchetti, F. C. Marincola, A.  
752 Kempf, Flamelet LES of a semi-industrial pulverized coal furnace, Com-  
753 bustion and Flame 173 (2016) 39–56.
- 754 [15] J. Watanabe, K. Yamamoto, Flamelet model for pulverized coal com-  
755 bustion, Proceedings of the Combustion Institute 35 (2015) 2315–2322.
- 756 [16] H. Nicolai, T. Li, C. Geschwindner, F. di Mare, C. Hasse, B. Böhm, J.  
757 Janicka, Numerical investigation of pulverized coal particle group com-  
758 bustion using tabulated chemistry, Proceedings of the Combustion In-  
759 stitute 38 (2021) 4033–4041.
- 760 [17] R. Knappstein, G. Kuenne, A. Ketelheun, J. Köser, L. Becker, S. Heuer,  
761 M. Schiemann, V. Scherer, A. Dreizler, A. Sadiki, et al., Devolatilization  
762 and volatiles reaction of individual coal particles in the context of FGM  
763 tabulated chemistry, Combustion and Flame 169 (2016) 72–84.
- 764 [18] L. Dressler, F. L. Sacomano Filho, F. Ries, H. Nicolai, J. Janicka, A.  
765 Sadiki, Numerical prediction of turbulent spray flame characteristics  
766 using the filtered Eulerian stochastic field approach coupled to tabulated  
767 chemistry, Fluids 6 (2021) 50.
- 768 [19] G. Tufano, O. Stein, B. Wang, A. Kronenburg, M. Rieth, A. Kempf,

- 769 Coal particle volatile combustion and flame interaction. part I: Charac-  
770 terization of transient and group effects, *Fuel* 229 (2018) 262–269.
- 771 [20] G. Tufano, O. Stein, B. Wang, A. Kronenburg, M. Rieth, A. Kempf,  
772 Coal particle volatile combustion and flame interaction. part II: Effects  
773 of particle reynolds number and turbulence, *Fuel* 234 (2018) 723–731.
- 774 [21] D. Messig, M. Vascellari, C. Hasse, Flame structure analysis and flamelet  
775 progress variable modelling of strained coal flames, *Combustion Theory  
776 and Modelling* 21 (2017) 700–721.
- 777 [22] X. Wen, K. Luo, H. Jin, J. Fan, Numerical investigation of coal flamelet  
778 characteristics in a laminar counterflow with detailed chemistry, *Fuel*  
779 195 (2017) 232–242.
- 780 [23] K. Luo, H. Wang, J. Fan, F. Yi, Direct numerical simulation of pulver-  
781 ized coal combustion in a hot vitiated co-flow, *Energy & fuels* 26 (2012)  
782 6128–6136.
- 783 [24] Y. Bai, K. Luo, K. Qiu, J. Fan, Numerical investigation of two-phase  
784 flame structures in a simplified coal jet flame, *Fuel* 182 (2016) 944–957.
- 785 [25] T. Hara, M. Muto, T. Kitano, R. Kurose, S. Komori, Direct numerical  
786 simulation of a pulverized coal jet flame employing a global volatile mat-  
787 ter reaction scheme based on detailed reaction mechanism, *Combustion  
788 and Flame* 162 (2015) 4391–4407.
- 789 [26] M. Rieth, A. Kempf, A. Kronenburg, O. Stein, Carrier-phase DNS of  
790 pulverized coal particle ignition and volatile burning in a turbulent mix-  
791 ing layer, *Fuel* 212 (2018) 364–374.

- 792 [27] X. Wen, M. Rieth, A. Scholtissek, O. T. Stein, H. Wang, K. Luo, A. M.  
793 Kempf, A. Kronenburg, J. Fan, C. Hasse, A comprehensive study of  
794 flamelet tabulation methods for pulverized coal combustion in a turbu-  
795 lent mixing layer—part I: A priori and budget analyses, *Combustion*  
796 *and Flame* 216 (2020) 439–452.
- 797 [28] X. Wen, M. Rieth, A. Scholtissek, O. T. Stein, H. Wang, K. Luo, A.  
798 Kronenburg, J. Fan, C. Hasse, A comprehensive study of flamelet tab-  
799 ulation methods for pulverized coal combustion in a turbulent mixing  
800 layer—part II: Strong heat losses and multi-mode combustion, *Combustion*  
801 *and Flame* 216 (2020) 453–467.
- 802 [29] M. Rieth, A. M. Kempf, O. T. Stein, A. Kronenburg, C. Hasse, M.  
803 Vascellari, Evaluation of a flamelet/progress variable approach for pul-  
804 verized coal combustion in a turbulent mixing layer, *Proceedings of the*  
805 *Combustion Institute* 37 (2019) 2927–2934.
- 806 [30] T. Brosh, D. Patel, D. Wacks, N. Chakraborty, Numerical investigation  
807 of localised forced ignition of pulverised coal particle-laden mixtures: a  
808 direct numerical simulation (DNS) analysis, *Fuel* 145 (2015) 50–62.
- 809 [31] J. Krüger, N. E. Haugen, D. Mitra, T. Løvås, The effect of turbulent  
810 clustering on particle reactivity, *Proceedings of the Combustion Institute*  
811 36 (2017) 2333–2340.
- 812 [32] S. Farazi, J. Hinrichs, M. Davidovic, T. Falkenstein, M. Bode, S. Kang,  
813 A. Attili, H. Pitsch, Numerical investigation of coal particle stream ig-  
814 nition in oxy-atmosphere, *Fuel* 241 (2019) 477–487.

- 815 [33] A. Attili, P. Farmand, C. Schumann, S. Farazi, B. Böhm, T. Li, C.  
816 Geschwindner, J. Köser, A. Dreizler, H. Pitsch, Numerical simulations  
817 and experiments of ignition of solid particles in a laminar burner: Effects  
818 of slip velocity and particle swelling, *Flow, Turbulence and Combustion*  
819 (2020) 1–17.
- 820 [34] T. Li, P. Farmand, C. Geschwindner, M. Greifenstein, J. Köser, C. Schu-  
821 mann, A. Attili, H. Pitsch, A. Dreizler, B. Böhm, Homogeneous ignition  
822 and volatile combustion of single solid fuel particles in air and oxy-fuel  
823 conditions, *Fuel* 291 (2021) 120101.
- 824 [35] L. Cai, S. Kruse, D. Felsmann, H. Pitsch, A methane mechanism for oxy-  
825 fuel combustion: Extinction experiments, model validation, and kinetic  
826 analysis, *Flow Turbulence and Combustion* (2020).
- 827 [36] X. Wen, A. Shamooni, O. T. Stein, L. Cai, A. Kronenburg, H. Pitsch,  
828 A. M. Kempf, C. Hasse, Detailed analysis of early-stage NO<sub>x</sub> forma-  
829 tion in turbulent pulverized coal combustion with fuel-bound nitrogen,  
830 *Proceedings of the Combustion Institute* 38 (2021) 4111–4119.
- 831 [37] X. Wen, H. Nicolai, O. T. Stein, J. Janicka, A. Kronenburg, C. Hasse,  
832 Effects of air and oxy-fuel atmospheres on flamelet modeling of pollu-  
833 tant formation in laminar counterflow solid fuel flames, *Fuel* 285 (2021)  
834 119079.
- 835 [38] S. Farazi, A. Attili, S. Kang, H. Pitsch, Numerical study of coal parti-  
836 cle ignition in air and oxy-atmosphere, *Proceedings of the Combustion*  
837 *Institute* 37 (2019) 2867–2874.

- 838 [39] D. M. Grant, R. J. Pugmire, T. H. Fletcher, A. R. Kerstein, Chemical  
839 model of coal devolatilization using percolation lattice statistics, *Energy*  
840 & *Fuels* 3 (1989) 175–186.
- 841 [40] S. Jimenez, C. Gonzalo-Tirado, Properties and relevance of the volatile  
842 flame of an isolated coal particle in conventional and oxy-fuel combustion  
843 conditions, *Combustion and Flame* 176 (2017) 94–103.
- 844 [41] D. G. Goodwin, R. L. Speth, H. K. Moffat, B. W. Weber, *Cantera*:  
845 An object-oriented software toolkit for chemical kinetics, thermodynam-  
846 ics, and transport processes, <https://www.cantera.org>, 2021. Version  
847 2.5.1.
- 848 [42] C. D. Pierce, P. Moin, Progress-variable approach for large-eddy simula-  
849 tion of non-premixed turbulent combustion, *Journal of fluid Mechanics*  
850 504 (2004) 73–97.
- 851 [43] P. Wollny, B. Rogg, A. Kempf, Modelling heat loss effects in high  
852 temperature oxy-fuel flames with an efficient and robust non-premixed  
853 flamelet approach, *Fuel* 216 (2018) 44–52.
- 854 [44] A. Ketelheun, G. Kuenne, J. Janicka, Heat transfer modeling in the  
855 context of large eddy simulation of premixed combustion with tabulated  
856 chemistry, *Flow, turbulence and combustion* 91 (2013) 867–893.
- 857 [45] B. Fiorina, O. Gicquel, L. Vervisch, S. Carpentier, N. Darabiha, Pre-  
858 mixed turbulent combustion modeling using tabulated detailed chem-  
859 istry and pdf, *Proceedings of the Combustion Institute* 30 (2005) 867–  
860 874.

- 861 [46] T. Landenfeld, A. Sadiki, J. Janicka, A turbulence-chemistry interaction  
862 model based on a multivariate presumed beta-pdf method for turbulent  
863 flames, *Flow, turbulence and combustion* 68 (2002) 111–135.
- 864 [47] C. Olbricht, O. Stein, J. Janicka, J. Van Oijen, S. Wysocki, A. Kempf,  
865 Les of lifted flames in a gas turbine model combustor using top-hat  
866 filtered pfgm chemistry, *Fuel* 96 (2012) 100–107.
- 867 [48] L. Berger, K. Kleinheinz, A. Attili, F. Bisetti, H. Pitsch, M. E. Mueller,  
868 Numerically accurate computational techniques for optimal estimator  
869 analyses of multi-parameter models, *Combustion Theory and Modelling*  
870 22 (2018) 480–504.
- 871 [49] P. Trisjono, H. Pitsch, Systematic analysis strategies for the develop-  
872 ment of combustion models from DNS: A review, *Flow, Turbulence and*  
873 *Combustion* 95 (2015) 231–259.
- 874 [50] A. Moreau, O. Teytaud, J.-P. Bertoglio, Optimal estimation for large-  
875 eddy simulation of turbulence and application to the analysis of subgrid  
876 models, *Physics of fluids* 18 (2006) 105101.
- 877 [51] J. R. Fessler, J. D. Kulick, J. K. Eaton, Preferential concentration of  
878 heavy particles in a turbulent channel flow, *Physics of Fluids* 6 (1994)  
879 3742–3749.
- 880 [52] M. Obligado, T. Teitelbaum, A. Cartellier, P. Mininni, M. Bourgoïn,  
881 Preferential concentration of heavy particles in turbulence, *Journal of*  
882 *Turbulence* 15 (2014) 293–310.



- 883 [53] R. Monchaux, M. Bourgoïn, A. Cartellier, Analyzing preferential con-  
884 centration and clustering of inertial particles in turbulence, *International*  
885 *Journal of Multiphase Flow* 40 (2012) 1–18.
- 886 [54] S. Ying, G. Xu, C. Li, Z. Mao, Point cluster analysis using a 3D voronoi  
887 diagram with applications in point cloud segmentation, *ISPRS Interna-*  
888 *tional Journal of Geo-Information* 4 (2015) 1480–1499.
- 889 [55] J. A. Palmore Jr, O. Desjardins, Technique for forcing high reynolds  
890 number isotropic turbulence in physical space, *Physical Review Fluids*  
891 3 (2018) 034605.
- 892 [56] T. Lau, G. J. Nathan, in: 7th Australian Conference on Laser Diagnos-  
893 tics in Fluid Mechanics and Combustion, at Melbourne, Australia.
- 894 [57] P. Gualtieri, F. Picano, C. Casciola, Anisotropic clustering of inertial  
895 particles in homogeneous shear flow, *Journal of Fluid Mechanics* 629  
896 (2009) 25–39.
- 897 [58] X. Wen, M. Rieth, W. Han, J. H. Chen, C. Hasse, Investigation of the  
898 ignition processes of a multi-injection flame in a diesel engine environ-  
899 nment using the flamelet model, *Proceedings of the Combustion Institute*  
900 38 (2021) 5605–5613.
- 901 [59] S. Cant, Sb pope, turbulent flows, cambridge university press, cam-  
902 bridge, uk, 2000, 771 pp., *Combustion and Flame* 4 (2001) 1361–1362.
- 903 [60] S. Apte, K. Mahesh, T. Lundgren, Accounting for finite-size effects  
904 in simulations of disperse particle-laden flows, *International Journal of*  
905 *Multiphase Flow* 34 (2008) 260–271.

906 [61] B. Wang, A. Kronenburg, G. L. Tufano, O. T. Stein, Fully resolved dns of  
907 droplet array combustion in turbulent convective flows and modelling for  
908 mixing fields in inter-droplet space, *Combustion and Flame* 189 (2018)  
909 347–366.